Research in Nondestructive Evaluation, 20: 1–31, 2009

ISSN: 0934-9847 print/1432-2110 online
DOI: 10.1080/09349840802366617

Taylor & Francis
Taylor & Francis Group

COMPARATIVE STUDY OF ACTIVE THERMOGRAPHY TECHNIQUES FOR THE NONDESTRUCTIVE EVALUATION OF HONEYCOMB STRUCTURES

Clemente Ibarra-Castanedo,[1] Jean-Marc Piau,[1] Stéphane Guilbert,[1] Nicolas P. Avdelidis,[2] Marc Genest,[3] Abdelhakim Bendada,[1] and Xavier P. V. Maldague[1]

[1]Computer Vision and Systems Laboratory, Department of Electrical and Computer Engineering, University Laval, Quebec City, Quebec, Canada
[2]National Technical University of Athens, School of Chemical Engineering, Materials Science and Engineering Section, Zografou Campus, Athens, Greece
[3]National Research Council Canada, Institute for Aerospace Research, Ottawa, Ontario, Canada

In this article, the theoretical and experimental aspects of three active thermography approaches: pulsed thermography (PT), lock-in thermography (LT), and vibrothermography (VT), are discussed in relation to the nondestructive evaluation (NDE) of honeycomb sandwich structures. For this purpose, two standard specimens with simulated defects (delaminations, core unbonds, excessive adhesive, and crushed core) were tested, and results were processed, examined, and compared. As will be pointed out, the similarities and differences between these active approaches allow conclusions to be made about the most suitable approach for a particular application. In addition, results from NDE inspection by X-rays and c-scan ultrasounds are provided and discussed for reference.

Keywords: active infrared thermography, honeycomb sandwich structures, pulsed thermography, vibrothermography

1. INTRODUCTION

Active infrared thermography requires an external source of energy to induce a temperature difference between defective and nondefective areas in the specimen under examination. As illustrated in Fig. 1, a wide variety of energy sources are available and can be divided into optical, mechanical, electromagnetic, or other excitation forms. In this article, we are interested in the optical and mechanical excitation modes. In optical excitation, the energy is delivered to the surface by means of optical devices such as photographic flashes (for pulsed heat stimulation) or halogen lamps (for periodic heating). In mechanical excitation, the energy is injected into the specimen by means of mechanical oscillations, using

Address correspondence to Clemente Ibarra-Castanedo, Computer Vision and Systems Laboratory, Department of Electrical and Computer Engineering, Laval University, Pavillon Pouliot, Of. 1102-D, Quebec City, Quebec G1K 7P4, Canada. E-mail: IbarraC@gel.ulaval.ca

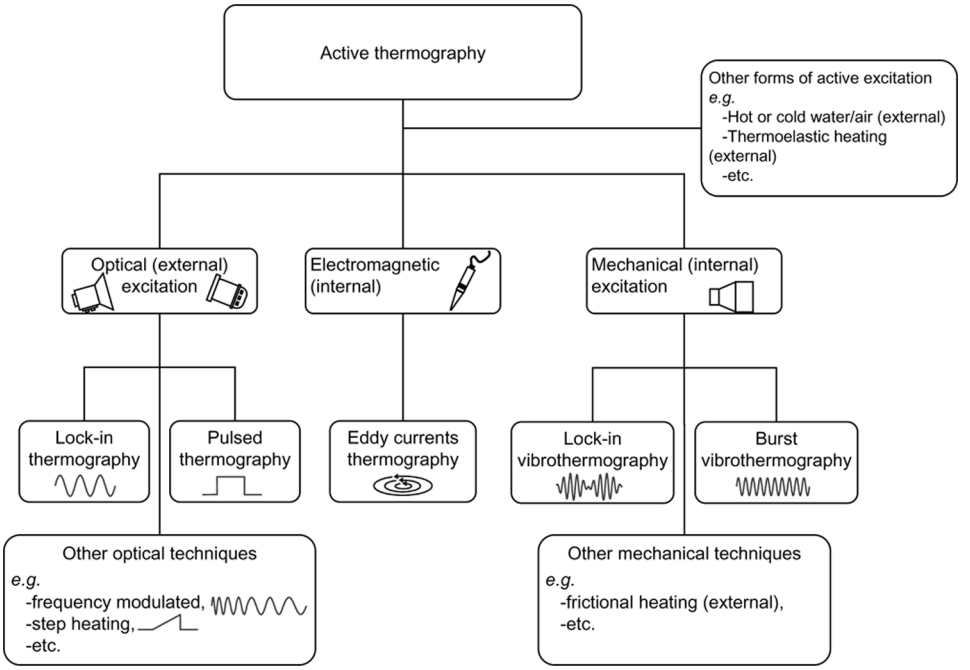

FIGURE 1. Active thermography methods.

for example a sonic or ultrasonic transducer. Optical excitation stimulates the defects externally, that is, the energy is delivered to the surface of the specimen where the light is transformed into heat. Thermal waves propagate by conduction through the specimen until they reach a discontinuity that either slows down or speeds up the propagation of the thermal waves (depending on the thermal properties of both the specimen and the discontinuity), which appear as a hot or cold spot on the specimen's surface. Mechanical excitation on the other hand, heats up the defects *internally*, that is, the mechanical oscillations injected into the specimen spread in all directions dissipating their energy at the discontinuities in the form of heat, which travels to the surface by conduction.

There are three classical active thermographic techniques based on these two excitation modes: lock-in thermography (LT) and pulsed thermography (PT), which are optical techniques applied externally; and vibrothermography (VT), which uses sonic or ultrasonic waves (pulsed or amplitude modulated) to excite surface or internal features. The experimental and theoretical aspects are different for each of these techniques and so are the typical applications. These techniques are described in the following paragraphs discussing their applicability to honeycomb sandwich structures.

2. PT

PT is one of the simplest and fastest nondestructive evaluation (NDE) techniques that does not require a physical contact with the specimen being inspected. PT is however affected by a variety of problems such as reflections from the environment, emissivity variations, nonuniform heating, and surface geometry variation. It is possible to have control over some of these effects. For instance, *painting* the specimen surface reduces environmental reflections and increases emissivity to nearly 1. However, other considerations escape from the user's control such as the surface condition and roughness, which might produce emissivity variations. Furthermore, the nonuniformity of the energy source is an unavoidable problem in the optical configuration that can only be minimized while carrying out the experiment and/or corrected through processing. Finally, there is not much control over the geometry of the inspected specimen, which might produce thermal artifacts in a similar manner as nonuniform heating. Several techniques can reduce the impact of some or all these problems. A succinct review of PT processing techniques is presented in Section 2.3. First, the basic theory behind PT is reviewed.

2.1. Theory

Heat diffusion through a solid is a complex 3D problem that can be described by Fourier's law of heat diffusion or the *heat equation* [1]:

$$\nabla^2 T - \frac{1}{\alpha} \cdot \frac{\partial T}{\partial t} = 0, \tag{1}$$

where ∇ is the 3D del operator (in the 3D Cartesian coordinate system is given by: $\nabla = i \cdot \partial/\partial x + j \cdot \partial/\partial y + k \cdot \partial/\partial z$), $\alpha = \mathrm{k}/\rho c_P$ [m^2/s] is the thermal diffusivity of the material being inspected, k [W/mK] its thermal conductivity, ρ [kg/m^3] its density, and c_P [J/kgK] its specific heat at constant pressure.

The 1D solution of the Fourier equation for the propagation of a *Dirac* heat pulse, that is, an ideal waveform defined as an intense unit-area pulse of so brief duration that no measuring equipment is capable of distinguishing it from even shorter pulses [2], in a semi-infinite homogeneous and isotropic solid by conduction has the form [1]:

$$T(z,t) = T_0 + \frac{Q}{e\sqrt{\pi t}} \exp\left(-\frac{z^2}{4\alpha t}\right), \tag{2}$$

where Q [J/m^2] is the energy absorbed by the surface, T_0 [K] is the initial temperature, $e = (k\rho c_\mathrm{P})^{1/2}$[m] is the effusivity, which is a thermal property that measures the material ability to exchange heat with its surroundings.

A Dirac heat pulse is composed of periodic waves at *all* frequencies and amplitudes. However, it is not possible to reproduce such a waveform.

In practice, a heat pulse provided by a powerful source such as a photographic flash has *approximately* a square shape (see [3] for a discussion on the real pulse shape). In this case, the signal is composed of periodic waves at *several* frequencies. The shorter the pulse, the broader the range of frequencies. At the surface ($z = 0$ mm), Eq. (2) can be rewritten as follows [1]:

$$T(0,t) = T_0 + \frac{Q}{e\sqrt{\pi t}}. \tag{3}$$

Although Eq. (3) is only an approximation of the complex 3D diffusion problem described by Fourier's law—Eq. (1)—many of the PT processing techniques have been based on this simplification to perform qualitative and quantitative analysis.

The following section discusses the experimental aspects of data acquisition by PT.

2.2. Data Acquisition

Data acquisition in PT is fast and straightforward as illustrated in Fig. 2 (top). The specimen surface is submitted to a heat pulse using a high power source such as photographic flashes. As time elapses, the thermal front will

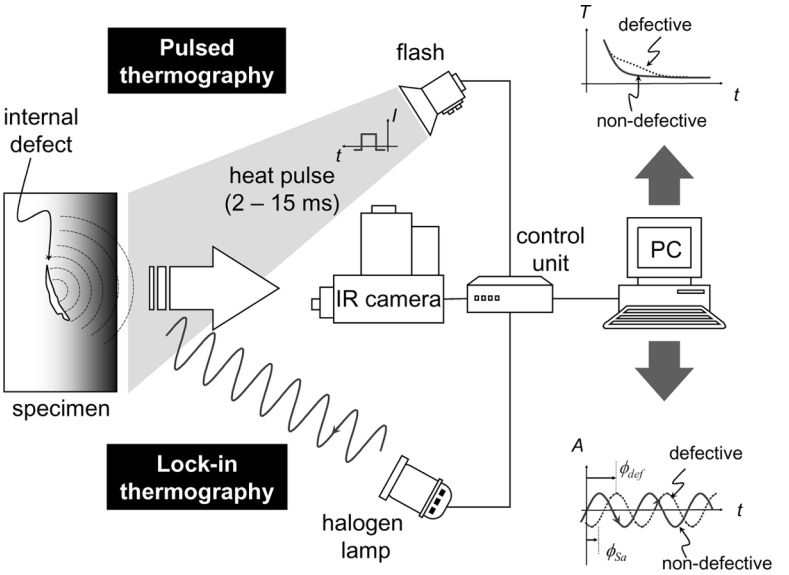

FIGURE 2. Optical techniques: pulsed thermography uses a flash and lock-in thermography uses a modulated lamp.

travel through the specimen, and the surface temperature will then decrease *uniformly* over time without flaws. On the contrary, subsurface discontinuities, such as porosity, delaminations, disbonds, fibre breakage, inclusions, etc., can be thought of as resistances to heat flow that produce abnormal temperature patterns at the surface, the thermal changes can be detected with an infrared camera and recorded for later analysis. A synchronization unit is needed to control the time between the launch of the thermal pulse and the recording. Data is stored as a 3D matrix where x and y are the spatial coordinates, and t is the time. Temperature decreases approximately as $t^{1/2}$ (at least at early times), as predicted by Eq. (3), except for the defective areas, where the cooling rate is different, as seen in Fig. 2. Once the data is acquired, it is available for qualitative and quantitative analysis.

2.3. Processing

PT is probably the most extensively investigated approach because of its ease of deployment. Nevertheless, raw PT data is difficult to handle and analyze. There are a great variety of processing techniques [4–7]. We selected four techniques that have shown very promising results when working with honeycomb sandwich structures.

Differentiated Absolute Contrast (DAC) Calculating thermal contrast is a basic operation that despite its simplicity is at the origin of many PT algorithms. Various thermal contrast definitions exist [4], but they all share the need for specifying a sound area S_a, that is, a nondefective region. For instance, the *absolute* thermal contrast ΔT(t) is defined as [4]:

$$\Delta T(t) = T_d(t) - T_{S_a}(t) \tag{4}$$

with $T_d(t)$ the temperature of a pixel or the average value of a group of pixels on a defective area at time t, and $T_{S_a}(t)$ the temperature at time t for the S_a. No defect can be detected at a particular t if $\Delta T(t) = 0$. However, in practice, raw data is contaminated with noise and other signal degradations [4], and a threshold of detectability ($\Delta T(t) > 0$) is generally established.

The main drawback of classical thermal contrast is establishing S_a, especially if an automated analysis is intended. Even when S_a definition is straightforward, considerable variations in the results are observed when the location of S_a is changed [8].

In the DAC method [9,10], instead of looking for a nondefective area, an *ideal* S_a temperature at time t is computed locally assuming that on the first few images (at least one image at time t' in particular, see below) this local point behaves as a S_a in accordance to Eq. (3), that is, there is no visible defect. The first step is to define t' as a given time value between the instant when the pulse has been launched, and the precise moment when the first

defective spot appears in the thermogram sequence, that is, when there is enough contrast for the defect to be detected. At t', there is no indication of the existence of a defect yet. Therefore, the local temperature for a S_a is exactly the same as for a defective area [10]:

$$T_{S_a}(t') = T_d(t') = \frac{Q}{e\sqrt{\pi t'}}. \tag{5}$$

By substituting Eq. (5) into the absolute contrast definition, Eq. (4), it follows that [10]:

$$\Delta T_{dac} = T_d(t) - \sqrt{\frac{t'}{t}} \cdot T(t'). \tag{6}$$

Actual measurements diverge from the solution provided by Eq. (6) for later times and as the plate thickness increases with respect to the nonsemi-infinite case. Nevertheless, the DAC technique has proven to be very efficient as it reduces the artefacts caused by non-uniform heating and surface geometry even for the case of anisotropic materials at early times [5]. Proper selection of t' requires an interactive procedure, for which a graphical user interface was developed [11], although automation is also possible [12]. Furthermore, a modified DAC technique has been proposed [13]. It is based on a finite plate model and the thermal quadrupoles theory that includes the plate thickness L explicitly in the solution to extend the validity of the DAC algorithm to later times. The Laplace inverse transform is used to obtain a solution of the form [13]:

$$\Delta T_{dac,mod} = T_d(t) - \frac{\mathcal{L}^{-1}\left[\coth\sqrt{pL^2/\alpha}\right]_t}{\mathcal{L}^{-1}\left[\coth\sqrt{pL^2/\alpha}\right]_{t'}} \cdot T(t'), \tag{7}$$

where p is the Laplace variable.

2.3.2. Thermographic Signal Reconstruction (TSR) Thermographic signal reconstruction (TSR) [14–16] is an attractive technique that reduces high frequency temporal noise, while decreasing the amount of data to be manipulated. TSR is based on the assumption that temperature profiles for nondefective pixels should follow the decay curve given by the 1D solution of the Fourier equation—Eq. (3)—which may be rewritten in the logarithmic form as [14]:

$$\ln(\Delta T) = \ln\left(\frac{Q}{e}\right) - \frac{1}{2}\ln(\pi t). \tag{8}$$

As stated before, Eq. (3) is only an approximation of the solution for the Fourier equation. To fit the thermographic data, Shepard [15] proposed to expand the logarithmic form into a series by using a m-degree polynomial

of the form:

$$\ln(\Delta T) = a_0 + a_1 \ln(t) + a_2 [\ln(t)]^2 + \cdots + a_m [\ln(t)]^m. \tag{9}$$

The thermal profiles corresponding to nondefective areas in the sample will approximately follow a linear decay, while a defective area will diverge from this linear behavior. Typically, m is set to 4 or 5 to assure a good correspondence between acquired data and fitted values while reducing the noise content in the signal. This is true when working with homogeneous and isotropic materials, for which thermal profiles approximate the model described by Eq. (8). Nevertheless, higher degree polynomials, typically 7 to 9, are often required when working with nonhomogeneous and anisotropic materials to fit the thermal profiles at later times (see for instance the experimental results presented in Section 5.4). At the end, the entire raw thermogram sequence is reduced to $m+1$ coefficient images (one per polynomial coefficient) from which *synthetic* thermograms can be reconstructed.

Synthetic data processing brings interesting advantages such as: significant noise reduction, possibility for analytical computations, and data compression (from N to $m+1$ images). As well, analytical processing provides the possibility of estimating the *actual* temperature for a time between acquisitions from the polynomial coefficients. Furthermore, the calculation of first and second time derivatives from the synthetic coefficients is straightforward [16]. The first time-derivative indicates the rate of cooling while the second time-derivative refers to the rate of change in the rate of cooling. Therefore, time derivatives are more sensitive to temperature changes than raw thermal images. There is no purpose using derivatives of higher order because there is a lack of a physical interpretation, and no further defect contrast improvement can be observed. Finally, TSR synthetic data can be used in combination with other algorithms to perform quantitative analysis as described at the end of the next section.

2.3.3. Pulsed Phase Thermography (PPT) In pulsed phase thermography (PPT) [17–19], data is transformed from the time domain to the frequency spectra using the one-dimensional discrete Fourier transform (DFT) [2]:

$$F_n = \Delta t \sum_{k=0}^{N-1} T(k\Delta t) \exp^{(-j2\pi nk/N)} = \mathrm{Re}_n + \mathrm{Im}_n, \tag{10}$$

where j is the imaginary number ($j^2 = -1$), n designates the frequency increment ($n = 0,1,\ldots,N$), Δt is the sampling interval, and Re and Im are the real and the imaginary parts of the transform, respectively.

Real and imaginary parts of the complex transform are used to estimate the amplitude A, and the phase ϕ, [17]:

$$A_n = \sqrt{\mathrm{Re}_n^2 + \mathrm{Im}_n^2} \tag{11}$$

$$\phi_n = \tan^{-1}\left(\frac{\mathrm{Im}_n}{\mathrm{Re}_n}\right). \tag{12}$$

Although very useful, Eq. (10) is slow. Fortunately, the fast Fourier transform (FFT) algorithm is available [20] to be implemented or can be found (integrally or simplified) in common software packages. DFT can be applied to *any* waveform, hence it can be used with lock-in and VT data [21], which will be discussed later in the paper.

The phase, Eq. (12), is of particular interest in NDE given that it is less affected than raw thermal data by environmental reflections, emissivity variations, nonuniform heating, and surface geometry and orientation. These phase characteristics are very attractive not only for qualitative inspections but also for quantitative characterization of materials. For instance, a depth inversion technique using the phase from PPT has been proposed [22]. The technique relies on the thermal diffusion length equation, defined as: $\mu = (\alpha/\pi \cdot f)^{1/2}$, in a manner similar to LT (see Section 3.3). The phase contrast has been proposed to determine the depth z [22], but automatic determination without sound area definition is also possible [23].

The noise content in phase data is considerable, especially at high frequencies. This causes a problem for the determination of the blind frequency f_b, which is defined as the limiting frequency at which a defect located at a particular depth presents enough phase (or amplitude) contrast to be detected in the frequency spectra and it is used for depth quantification with the phase (see Section 3.3). A de-noising step is therefore often required. The combination of PPT and TSR has proven to be very effective for this matter, reducing noise and allowing the depth retrieval of defects [24]. An example is shown in Section 5. Another difficulty is that, given the time-frequency duality of the Fourier transform, special care must be given to the selection of the sampling and truncation parameters prior to the application of the PPT. These two parameters depend on the thermal properties of the material and on the depth of the defect, which are often precisely the subject of the investigation. An interactive procedure has been proposed for this matter [25]. The importance of the sampling and truncation parameters will be highlighted in one of the examples presented in Section 5.

As a final note, the FFT is typically used to extract amplitude and phase information in PPT. Nevertheless, it is also possible to use different transformation algorithms such as wavelet transforms [26–28].

2.3.4. Principal Component Thermography (PCT) As explained above, the Fourier transform provides a valuable tool to convert the signal from the *temperature-time* space to a *phase-frequency* space, but it does so through the use of sinusoidal *basis functions*, which may not be the best choice for representing transient signals, which are the temperature profiles typically found in PT. Singular value decomposition (SVD) is an alternative tool to extract spatial and temporal data from a matrix in a compact or simplified manner. Instead of relying on a basis function, SVD is an eigenvector-based transform that forms an *orthonormal* space. SVD is close to principal component analysis (PCA) with the difference that SVD simultaneously provides the PCAs in both row and column spaces.

The SVD of an $M \times N$ matrix $\mathbf{A}$ ($M > N$) can be calculated as follows [29]:

$$\mathbf{A} = \mathbf{U}\mathbf{R}\mathbf{V}^{\mathrm{T}}, \tag{13}$$

where $\mathbf{U}$ is a $M \times N$ orthogonal matrix, $\mathbf{R}$ being a diagonal $N \times N$ matrix (with singular values of $\mathbf{A}$ present in the diagonal), and $\mathbf{V}^{\mathrm{T}}$ is the transpose of an $N \times N$ orthogonal matrix (characteristic time).

Hence, in order to apply the SVD to thermographic data, the 3D thermogram matrix representing time and spatial variations has to be reorganised as a 2D M *x* N matrix $\mathbf{A}$. This can be done by rearranging the thermograms for every time as columns in $\mathbf{A}$, in such a way that time variations will occur column-wise while spatial variations will occur row-wise. Under this configuration, the columns of $\mathbf{U}$ represent a set of orthogonal statistical modes known as empirical orthogonal functions (EOF) that describes spatial variations of data [30,31]. On the other hand, the principal components (PCs), which represent time variations, are arranged row-wise in matrix $\mathbf{V}^{\mathrm{T}}$. The first EOF will represent the most characteristic variability of the data; the second EOF will contain the second most important variability, and so on. Usually, original data can be adequately represented with only a few EOFs. Typically, a 1,000 thermogram sequence can be replaced by 10 or less EOFs.

The four techniques just described are intended to process PT data. As discussed next, LT signals behave differently.

3. LT

3.1. Theory

LT, also known as *modulated thermography* [32], is a technique derived from *photothermal radiometry* [33] in which a small surface spot is periodically illuminated by a modulated laser beam to inject thermal waves into the specimen. The thermal response is recorded at the same time using an

infrared detector and decomposed by a lock-in amplifier to extract the amplitude and phase of the modulation [34]. Photothermal radiometry is a point technique that requires long acquisition times especially in the case of deep defects involving very low modulation frequencies. Furthermore, extra hardware such as lock-in amplifier was needed in order to retrieve the amplitude and phase of the response.

Fortunately, it is possible to dramatically simplify and speed up the acquisition process for NDT applications. LT [35] replaces: (1) the laser beam with one or several modulated heating sources, halogen lamps for example, that cover the entire specimen surface instead of only a point; (2) the infrared detector with an infrared camera capable of monitoring large surface areas (typically in a 320 x 256 or 640 x 512 pixel matrix configuration); and (3) the lock-in hardware with a software capable of recovering mathematically the amplitude and phase of the response.

Sinusoidal waves are typically used in LT, although it is possible to use other periodic waveforms. Using sinusoids as input has the advantage that the frequency and shape of the response are preserved; only the amplitude and phase delay of the wave may change, which is known as sinusoidal fidelity. The periodic wave propagates by radiation through the air until it reaches the specimen surface where the heat is produced that propagates through the material. Internal defects act as barriers for heat propagation, which produces changes in the amplitude and phase of the response signal at the surface of the item under inspection.

The 1D solution of the Fourier's law—Eq. (1)—for a periodic thermal wave propagating through a semi-infinite homogeneous material may be expressed as [36]:

$$T(z,t) = T_0 \exp\left(-\frac{z}{\mu}\right) \cos\left(\frac{2\pi \cdot z}{\lambda} - \omega t\right), \tag{14}$$

where T_0 [°C] is the initial change in temperature produced by the heat source, $\omega = 2\pi f$ [rad/s] is the modulation frequency, f [Hz] is the frequency, $\lambda = 2\pi\mu$ [m] is the thermal wavelength, and μ [m] is the thermal diffusion length, which determines the decay rate of the thermal wave as it penetrates through the material and is defined by [36]:

$$\mu = \sqrt{\frac{2 \cdot \alpha}{\omega}} = \sqrt{\frac{\alpha}{\pi \cdot f}}. \tag{15}$$

Equation (15) states that thermal waves propagate deeper in more diffusive materials but information about deeper features is available at lower frequencies. As pointed out next, these two aspects are important to know when planning the inspection of a part in order to adequately select the frequency and to determine the depth of internal defects.

3.2. Data Acquisition

LT is an optical technique depicted in Fig. 2 (bottom). One lamp is shown although it is possible to use several lamps mounted on a frame to reduce the nonuniform heating, to increase the amount of energy delivered to the surface, or both. The lamps send periodic waves (sinusoids for example) at a given modulation frequency ω, for at least one cycle, ideally until a steady state is achieved, which depends on the specimen thermal properties and the defect depth, see Eq. (15). However, in practice, only a few cycles are needed to adequately retrieve the phase and amplitude data, which is long before attaining steady state conditions.

3.3. Processing

A four point methodology for sinusoidal stimulation is available [35,37]. As mentioned before, input and output have the same shape when sinusoids are used. There is only a change in amplitude and phase that can be calculated as [37]

$$A = \sqrt{(S_1 - S_3)^2 + (S_2 - S_4)^2} \tag{16}$$

$$\phi = \tan^{-1}\left(\frac{S_1 - S_3}{S_2 - S_4}\right). \tag{17}$$

The 4-point method is fast. However, it is valid only for sinusoidal stimulation and is affected by noise. The signal can be de-noised in part by averaging several points instead of a single one, by increasing the number of cycles, or both. Another possibility is to fit the experimental data using least squares regression [38] and to use this synthetic data to calculate the amplitude and the phase. Nevertheless, these two alternatives considerably slow down the calculations and the obtained results are far from perfect. Alternatively, the DFT can be used to extract amplitude and phase information from LT data through Eqs. (11) and (12), as is done in PT data [17] (see Section 2.3.3).

One of the most interesting characteristics of LT testing is the possibility of performing straightforward quantitative operations. A direct relationship exists between the depth of a defect and the thermal diffusion length, μ, which can be exploited through a relationship of the form [22]

$$z = C_1 \cdot \mu = C_1 \sqrt{\frac{\alpha}{\pi \cdot f_b}}, \tag{18}$$

where C_1 is an empirical constant and f_b [Hz] is the blind frequency [39], which is discussed in Section 2.3.3. The inversion problem in LT (and PPT) is reduced to the estimation of f_b from the phase.

Several experimental investigations have been carried out on this matter [39–45]. It has been observed that $C_1 = 1$ when using amplitude data [42], whilst reported values when working with the phase are in the range $1.5 < C_1 < 2$ [25–29] with $C_1 = 1.82$ typically adopted [43–45].

The phase is of more interest in NDT than the amplitude, since it provides deeper probing capabilities. A reason for this is the ratio involved in Eq. (12), which cancels part of the artefacts related to nonuniform heating, environmental reflections, emissivity variations, and surface geometry variations. PPT results agree with these numbers for homogeneous materials [22]: $C_1 \sim 1.72$ for steel, and $C_1 \sim 2.0$ for Plexiglas®, and for anisotropic materials [25]: $C_1 \sim 1.73$ for CFRP.

4. VT

4.1. Theory

VT, also known as *ultrasound thermography* [21] or *thermosonics* [46], utilizes mechanical waves to directly stimulate internal defects without heating the surface as in optical methods (*e.g.*, LT, PT). If optical LT is considered to be the successor of photothermal radiometry as mentioned before, VT can be seen as the successor of *optoacoustics* or *photoacoustics* [42,47,48], in which microphones or piezoceramics in contact with the specimen and a lock-in amplifier were used to detect the thermal wave signature from a defect. This was performed in a point-by-point manner and lacked practical interest at the time. The theory behind however, was the base for the later development of VT.

Sonic waves, audible for humans, vibrate between 20 Hz and 20 kHz. The range for ultrasonic waves, not audible to humans, is between 20 kHz and 1 MHz, although most transducers used in VT operate between 15 and 50 kHz. Unlike electromagnetic waves, mechanical elastic waves such as sonic and ultrasonic waves do not propagate in a vacuum; on the contrary, they require a medium to travel. They travel faster in solids and liquids than through the air. This brings about an important aspect of ultrasonic systems: although contactless (through air) ultrasound is currently under intense investigation in many areas [49], the common approach is to use a coupling media such as a piece of fabric, water-based gels, or aluminium, between the transducer and the specimen to reduce losses.

In the classical ultrasound C-scan NDT inspection, a transducer is placed in contact with the sample with the help of a coupling media (water or water-based gels). The ultrasonic waves travel through the specimen and are transmitted back to the surface where the transducer picks up the reflected signal (pulse-echo technique), or they are collected on the opposite side (through transmission). In any case, the principle of defect detection is based on the differences in specific acoustic impedances (Z) between materials. In VT, the ultrasonic waves will travel freely through a homogeneous material,

whereas an internal defect will produce a complex combination of absorption, scattering, beam spreading, and dispersion of the waves, whose principal manifestation will be in the form of heat. The heat generated will then travel by conduction in all directions. An IR camera can be directed to one of the surfaces of the specimen to capture the defect signature.

Ultrasonic waves are ideal for NDT as the defect detection is independent from of its orientation inside the specimen, and both internal and open surface defects can be detected. Hence, VT is very useful for the detection of cracks and delaminations.

The next paragraph describes the experimental setup of a VT experiment.

4.2. Data Acquisition

Two VT configurations can be considered as analogues to optical methods described above. The first one is *lock-in* VT (or amplitude modulated VT), analogue to the LT approach; and the second technique is *burst* VT, which is somewhat analogous to PT. These two approaches are illustrated in Fig. 3.

It should be mentioned that is also possible to either modulate the frequency (in addition to the amplitude) in lock-in or burst VT [50]. This procedure is often called *wobbulation*. The idea is to cover a range of ultrasonic frequencies in a single experiment, instead of only one, since it is not always possible to predict the right frequency for a particular application. Ultrasonic wobbulation can be compared to a heat pulse, which is composed of thermal

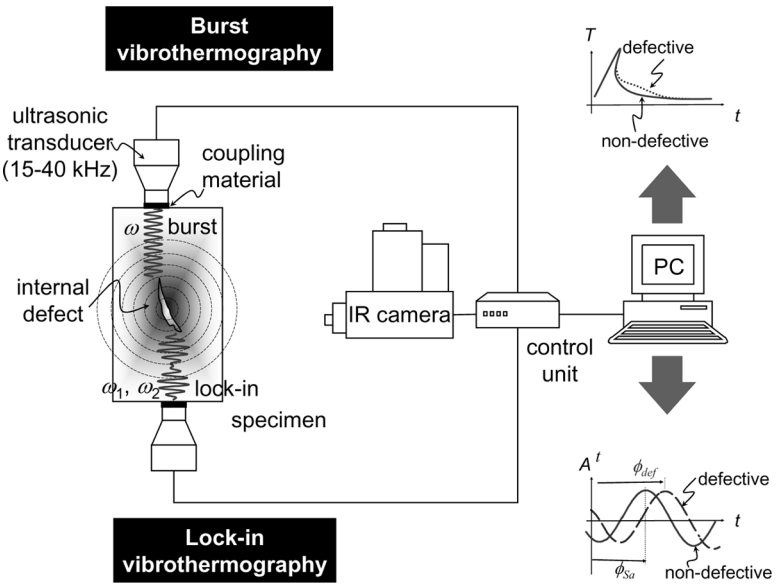

FIGURE 3. Mechanical techniques: vibrothermography can be carried out in either burst or lock-in mode.

waves at many frequencies. In this sense, wobbulated burst VT would be a better analogue technique to PT. Wobbulation is interesting to prevent the appearance of *standing waves*, which are produced when working at the natural harmonic resonance frequencies of the material (see, for instance, the wave patterns in TYPE I defects in Fig. 12). However, it is sometimes preferable to repeat the acquisition at different frequencies whenever results are contaminated with standing waves.

The ultrasound wave is produced by a transducer made of a stack of piezoelectric elements and concentrated in a titanium horn that acts like a hammer. Hence, the part being inspected should be firmly immobilized (but without damaging it) to avoid cantilever effects, clapping, and sliding of the transducer. The transducer horn should be pressed against the sample as well to improve the coupling of the ultrasound into the specimen. Insertion of a material between the transducer and the sample is strongly recommended, not only as a coupling medium but also to avoid damaging the sample and to correct misalignment. A bad coupling implies a poor ultrasound transmission and creates unwanted heat near the ultrasound injection point.

After the elastic waves are injected into the specimen, they travel through the material and dissipate their energy mostly at the defect boundaries so heat is locally released. The thermal waves then travel by conduction to the surface, where they can be detected with an IR camera.

VT is very fast since, in general, no temporal processing is required, and the acquisition ends as soon as the defect appears. A typical VT experiment lasts a fraction of a second, which is even faster than PT. This is good because the longer the transducer operates at the surface, the more heat is released at the contact surface, thus increasing the probability of damaging the area. Additionally, the pressure applied between the horn and the specimen has a great impact on the thermal response [51].

4.3. Processing

Results obtained by VT, either burst or lock-in, strongly depend on the experimental conditions. If the correct parameters are chosen for the acquisition, signal processing is minimal. Cold image subtraction is commonly used. As in the case of PT and LT, the FFT algorithm can be used to recover the amplitude and phase images through Eqs. (11) and (12).

5. EXPERIMENTAL RESULTS

5.1. Apparatus

The acquisitions were carried out using an infrared camera (ThermaCAM™ Phoenix® from FLIR Systems,14 bits, InSb 640×512 FPA, 3–5 μm, Stirling closed cycle cooler), working at a sampling frequency of 88 Hz. For the PT experiments, two high-power flashes (Balcar FX 60, 6.4 kJ, 2 ms

pulse), were used as heating sources. A set of 6 heating lamps providing 1,000 W each was used as modulated heating source for LT tests.

For the VT inspections, two ultrasonic transducers were used to apply sound waves at frequencies, one working in the range 15–25 kHz, and the other one at 40 kHz exclusively. The ultrasonic horn pressed against the sample with a static pressure typically around 250 psi, and the excitation lasted from a few milliseconds (burst) to a few seconds (lock-in) only. Coupling material between the horn and the specimen was used to protect the specimen and to reduce energy losses. The sample was rigidly mounted using the minimal number of holding points to avoid any movement and was properly isolated with cork to avoid vibration losses.

5.2. Specimens

The specimens used in this article consisted of NDE standard aluminium honeycomb core sandwich panels, with five-ply (127 μm each) graphite

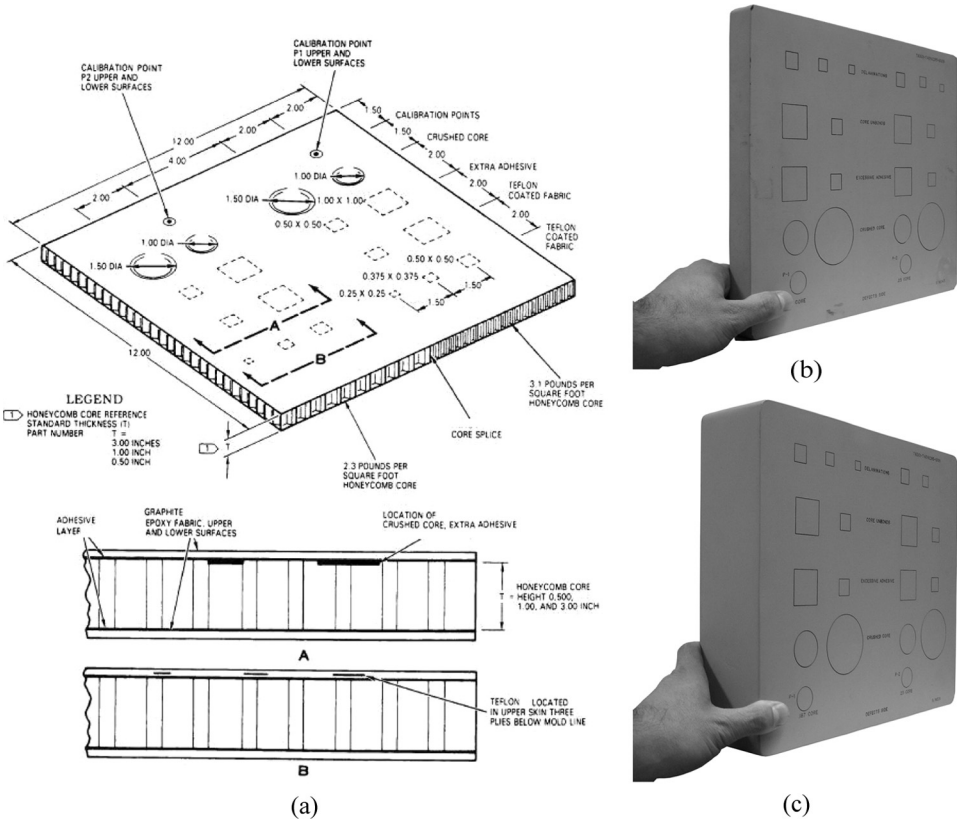

FIGURE 4. (a) Specifications for the calibration plates, (b) specimen SN043 (2.5 cm thick), and (c) specimen SN031 (7.6 cm thick).

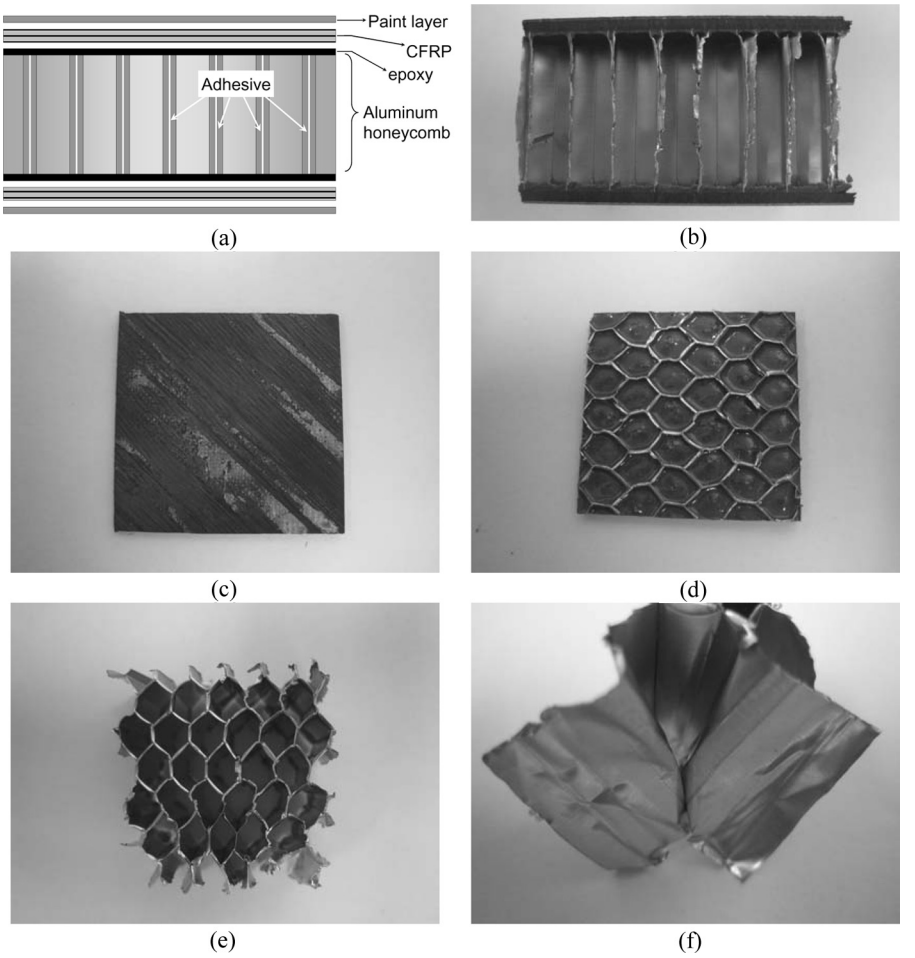

FIGURE 5. Typical honeycomb core sandwiched structure: (a) illustration, (b) cross section, (c) CFRP ply at 45° orientation, (d) inner part of the CFPR layer showing the residual adhesive material, (e) crushed honeycomb core, and (f) bonding between honeycomb cells.

epoxy face sheet (skin) as shown in Fig. 4. The aluminium honeycomb core has two cell densities, 11.2 kg/m^2 (2.3 lb/ft^2) on one side, and 15.1 kg/m^2 (3.1 lb/ft^2) on the other. The plate specifications are shown in Fig. 4a. They contain four types of fabricated defects. TYPE I: delaminations simulated using Teflon® coated fabric (CHR-3TB); TYPE II: skin unbonds fabricated using Teflon® coated fabric (CHR-6TB); TYPE III: excessive adhesive; and TYPE IV: crushed core. Figure 5 shows a typical honeycomb core sandwiched structure (not from the standard plates shown in Fig. 4) to give an idea of the nature of the specimen structure and the encountered defects. Two specimens were tested with the same defect distribution but different core thickness.

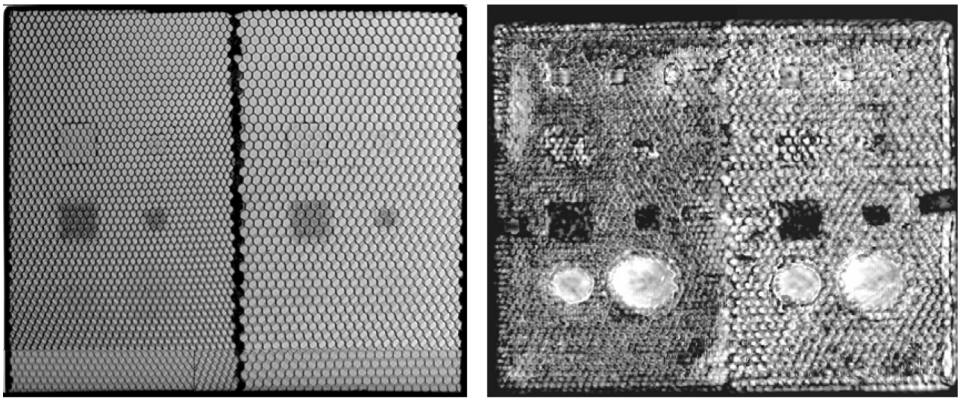

(a) (b)

FIGURE 6. Results for the 2.5 cm thick plate (specimen SN043): (a) X-rays, (b) Ultrasonic c-scan.

Specimen SN043 is 2.5 cm thick (Fig. 4b), and specimen SN031 is 7.6 cm (Fig. 4c).

5.3. Ultrasonic C-scan and X-rays

Specimen SN043 was inspected by ultrasonic c-scan and X-rays at the TWI Technology Centre in Wales, UK, and results are shown in Fig. 6. X-rays (Fig. 6a) allow seeing the honeycomb cells and the difference in core density between the left and right sides of the sample. However, only defects TYPE II (core unbonds) and TYPE III (excessive adhesive) were detected. Ultrasonic c-scan, on the contrary (Fig. 6b), allows detecting all four types of defects and the honeycomb cells but with lesser resolution. The two additional features through the line of TYPE III defects on both sides of the plate are supports used to hold the sample during the inspection.

Specimen SN031 was analyzed by ultrasonic c-scan testing at the Industrial Materials Institute of the National Research Council Canada in Boucherville, Quebec. Results are presented in Fig. 7. Five of the six TYPE I defects, that is, the simulated delaminations can be clearly seen in Fig. 7a. The rightmost delamination is missing since the specimen was not correctly centred during the inspection. The top figure shows the size and shape of the defects, whilst the bottom figure provides the information about their relative depth. For instance, it can be observed that the delaminations are near the specimen's surface and above the honeycomb core, which correspond with the information presented in Fig. 4, that is, the delaminations are three carbon fiber reinforced plastic (CFRP) plies below the surface. In addition, there are three spots in the area corresponding to

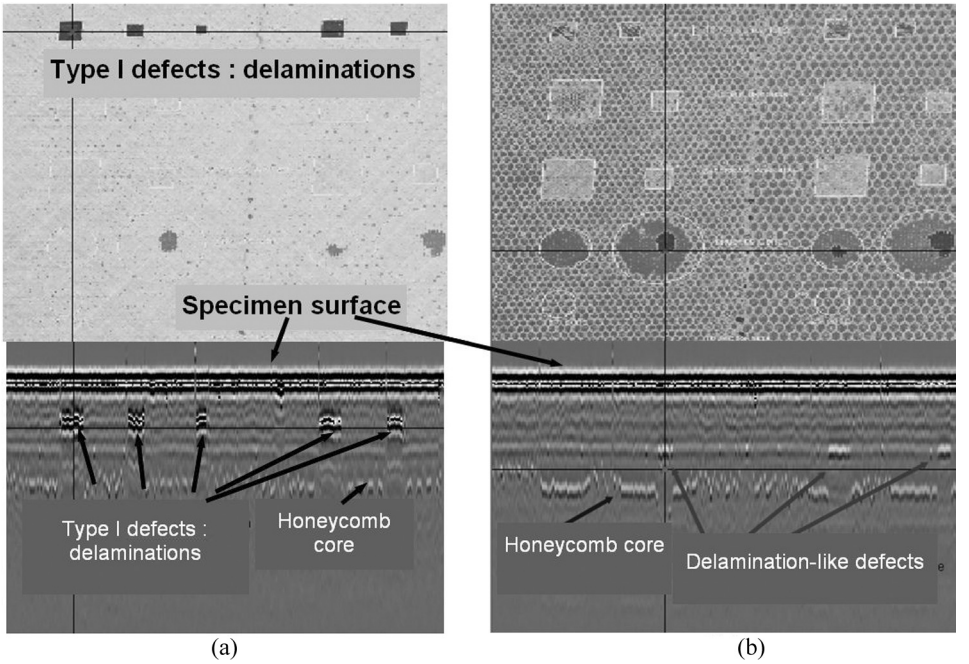

FIGURE 7. Ultrasonic c-scan inspection of the 7.6 cm thick plate (specimen SN031) showing: (a) simulated delaminations (Teflon® inserts) located 3 plies below skin, (b) defects (possibly delaminations) near the honeycomb structure.

the TYPE IV defects (crushed core circles), which were not present in the SN043 specimen. These unexpected marks, still visible in Fig. 7b (top), are deeper than the simulated delaminations, as seen in Fig. 7b (bottom). Furthermore, some surface features are present such as the defects indications and the inscriptions. Finally, the two different honeycomb densities can easily be distinguished.

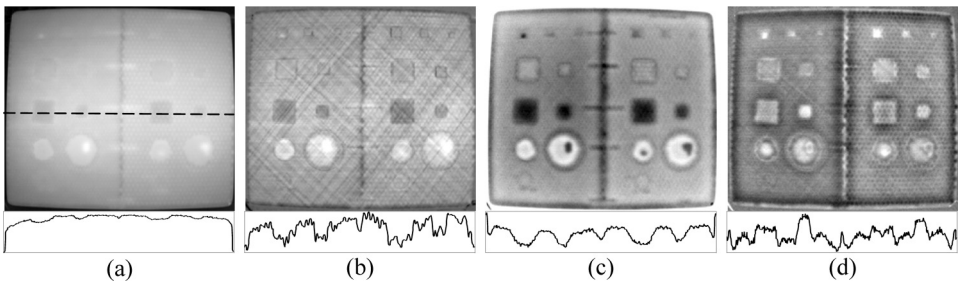

FIGURE 8. Processing results for the 7.6 cm thick plate (specimen SN031), inspected by pulsed thermography at $t = 2.5$ s: (a) raw data, (b) DAC, and (c) first, and (d) second time derivatives from a 7th degree polynomial.

5.4. Thermographic Comparative Results

Both specimens were inspected by PT, LT, and VT. Figure 8 presents some PT results. As is well-known, the maximum contrast of a defect depends on its depth and the thermal properties of both the defect and the specimen. The raw thermal contrast for TYPE I defects (delamination-like defects very thin and very near the surface) worsens rapidly after a few seconds of cooling. All the other defects are visible for longer time, starting early during cooling and ending after several seconds. Hence, the raw thermogram at $t = 2.5$ s (Fig. 8a), was selected as an appropriate instant to show all defects with good thermal contrast. Incidentally, this same instant is close to the best overall contrast image obtained by DAC and TSR (first and second derivative, see Fig. 17 in Section 5.5). Figures 8b–d show the results using the DAC technique, the first and second time derivatives (obtained from a 7th degree polynomial by TSR), respectively. Spatial profiles through a horizontal line at the center of the TYPE II defects (extra-adhesive) are also included at the bottom of all the results as an indication of relative defect contrast, noise presence, and nonuniform heating.

Some observations can be made from these results. The raw thermogram in Fig. 8a shows signs of nonuniform heating, which reduces the defect contrast. The fiber distribution is better seen in the DAC result of Fig. 8b. With the exception of the TYPE I (delaminations in the first row), defects are clearer in the first derivative result (Fig. 8c). The delaminations and the honeycomb matrix are best resolved in the second derivative image in Fig. 8d. This analysis is purely qualitative and based on a personal perception. In an effort to validate this observation, a signal-to-noise (SNR) analysis is presented in Section 5.5. It is shown here that the maximum SNR for the fourth delamination from the left is in fact higher for the first time derivative result ($t = 2.3$ s) than for the second time derivative ($t = 3.6$ s).

Figure 9 shows the phasegrams at four frequencies after applying the PPT algorithm to the raw thermogram sequence (top row), named *raw* PPT phase; and to a reconstructed sequence generated from a 7th degree polynomial obtained by TSR (central row), named *synthetic* PPT phase. As mentioned before, when working with anisotropic materials, a higher degree polynomial is required to accurately fit the experimental thermal profiles. Raw and synthetic phasegrams are very similar at low frequencies (Fig. 9a), where the levels of noise are much lower than the actual phase measurement. However, noise is more important at higher frequencies as seen in the spatial profiles (Figs. 9b,c). The advantage of using reconstructed data over raw thermal data in PPT is more evident in Fig. 9d, where the raw phasegram is covered with noise and only some of the defects can be seen, whilst the synthetic phasegram shows much more detail, fiber distribution in particular. It is important to recall at this point that deeper defects are seen at lower frequencies and vice-versa. Hence, it is normal to find information about the shallowest features in Fig. 9d.

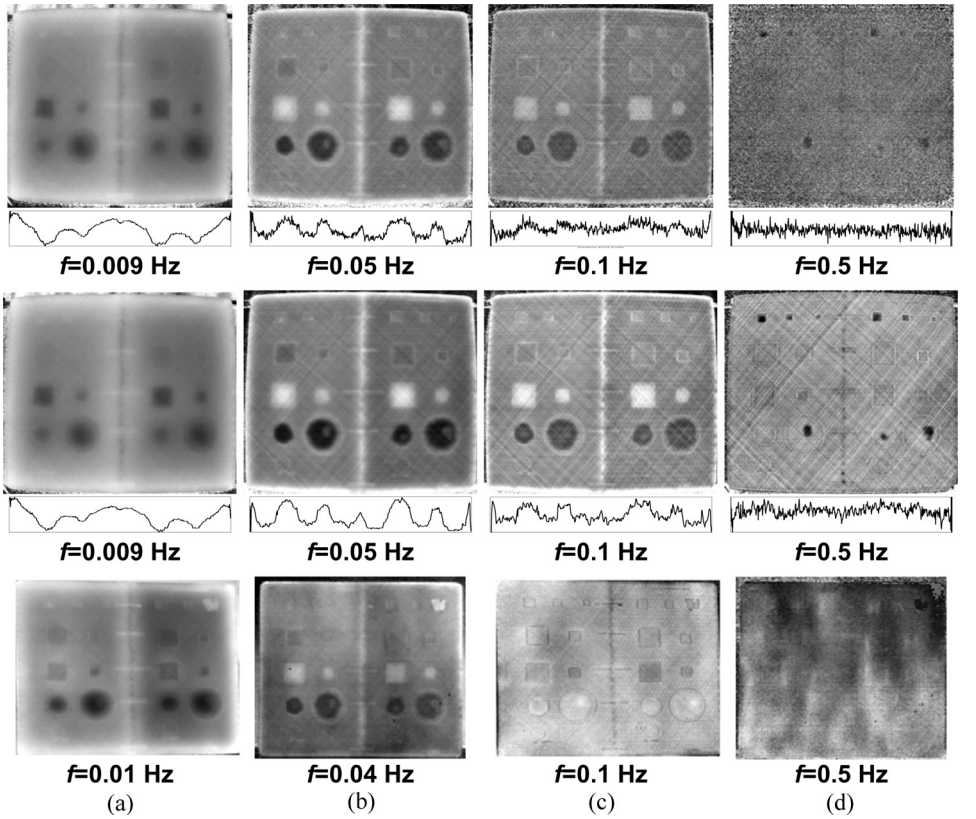

FIGURE 9. Phasegrams at different frequencies for the 7.6 cm thick plate (specimen SN031), inspected by lock-in thermography (top), pulsed phase thermography over raw data (center), and pulsed phase thermography over synthetic data from a 7th degree polynomial fitting (bottom).

The bottom row of Fig. 9 shows the phasegrams obtained by LT at approximately the same frequencies used in PPT. LT phasegrams are comparable to PPT results at the first three frequencies. However, the high frequency LT phasegram is different. An even lower frequency ($f = 0.005$ Hz) was tested by LT, the phasegram is shown in Fig. 10a. In addition, a portion of paint above the rightmost delamination was detached during the ultrasonic c-scan inspection, that is, prior to LT inspection as seen in Fig 10b. LT phasegrams show this surface feature. PPT results on the contrary, were obtained before the ultrasonic c-scan inspection; hence, they do not show any sign of paint detachment.

Figure 11 presents some results obtained by PCT. These images correspond to the first 5 EOFs after applying PCT to the entire sequence (the same sequence used in the PPT results, no windowing was used), higher order EOFs show mostly noise. PCT reorganizes data in a transformed space where the first component contains the maximum variance. It is interesting to see

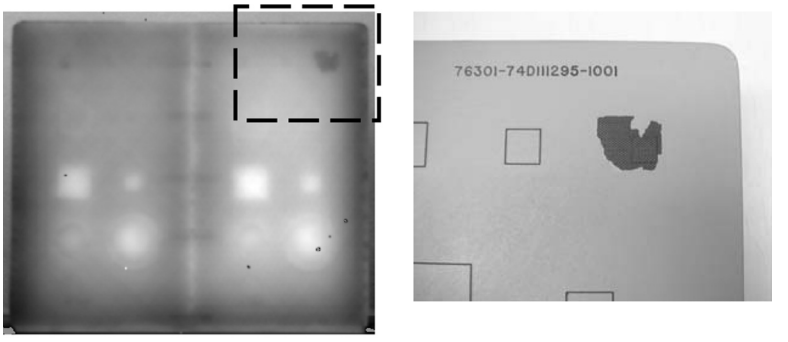

FIGURE 10. (a) IT phasegram at $f = 0.005$ Hz, and (b) cropped portion of the specimen SN031 showing a surface paint detachment.

that after applying the PCT, each of the resulting EOF highlights a specific type of feature or defect. For instance, nonuniform heating dominates the variance of the EOF_1 (only TYPE IV defects are visible, Fig. 11a) but is less palpable at higher order EOFs. On the contrary, most of the data variance in the EOF_2 is related to subsurface defect information, only TYPE I defects are difficult to detect since they are very thin (they are present in only a few thermograms of the sequence contrary to the thicker defects that are visible in several thermograms). EOF_3 in Fig. 11c shows more details about the honeycomb core, the CFRP fibre distribution, the TYPE I defects and even some surface features such as the printed inscriptions. The last two EOFs in Figs. 11d,e, complement the information about the subsurface defects and the fibre distribution.

Figure 12 presents a phasegram obtained by lock-in VT at a frequency of 2 Hz for 3 cycles. Most of the defects are visible. Some *standing waves*, that is, wave patterns that do not correspond to defects or to the honeycomb core, can be seen in the TYPE IV defects but nowhere else for this particular modulation frequency. It is difficult to distinguish the honeycomb core on the left side, which has a higher density. The right side honeycomb core on the

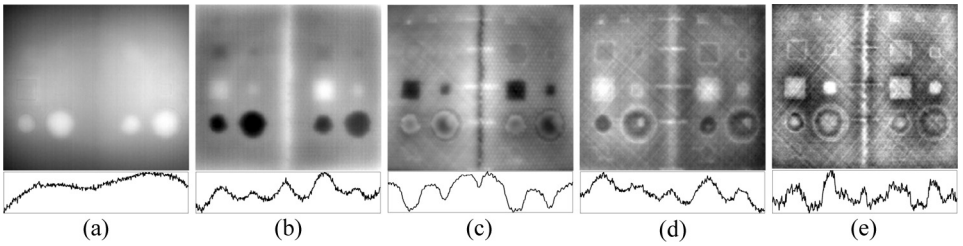

FIGURE 11. PCT results for the 7.6 cm thick plate (specimen SN031): (a) EOF_1, (b) EOF_2, (c) EOF_3, (d) EOF_4, and (e) EOF_5.

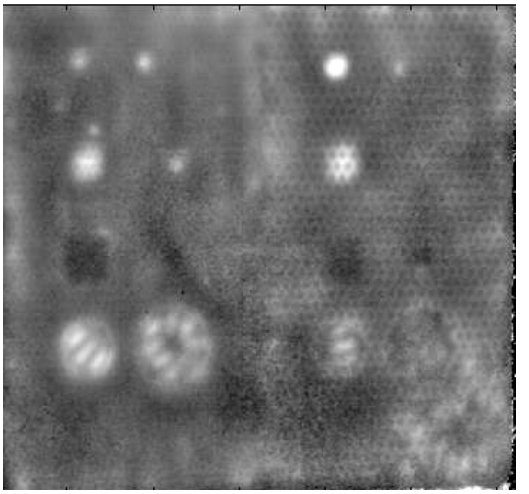

FIGURE 12. VT phasegram showing all four types of defects.

contrary can be seen in this image. The right lower corner of the plate was damaged during the preliminary tests of the VT inspection, which was carried out after all other inspection techniques were applied. Hence, previous results from thermographic techniques, ultrasonic c-scan and X-rays do not show any sign of the damage.

Although the specimen's skin is composed of 5 CFRP layers glued together, it is possible to estimate the depth of the TYPE I defects (delaminations) using

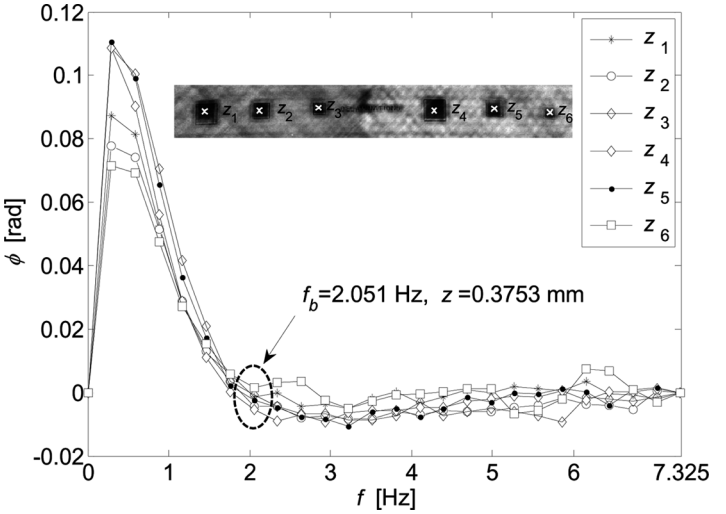

FIGURE 13. Phasegram showing the defect positions (top) and corresponding phase contrast profiles (bottom) for the six TYPE I defects (delaminations) in specimen SN043.

the PPT phase and Eq. (18), by considering the CFRP above the delaminations as a single layer with average thermal properties. For the depth estimation, the CFRP thermal properties found in the literature: $\alpha = 4.2 \times 10^{-7}\,\mathrm{m^2/s}$ [4], and a regression constant $C_1 = 1.47$ as reported in [22] are used. Figure 13 shows the phase contrast profiles for the 6 delaminations. Although some differences in the maximum phase contrast are observed, the blind frequency is practically the same for all defects regardless of their size. Using the discrete frequency value from the raw phase data, a depth value of $z = 0.375\,\mathrm{mm}$ was calculated, which is very close to the real depth, i.e., $z = 0.381\,\mathrm{mm}$, given in Fig. 4.

On the contrary, it is not possible to have an accurate estimation of the defect depth from PPT phase data of TYPE II, TYPE III, and TYPE IV defects (Figs. 14–16), since there is an additional adhesive layer approximately 0.3 mm thick in between the CFRP and the honeycomb. This structure behaves more like a multilayer structure for which it is not possible at the moment to perform quantitative analysis by PPT. Nevertheless, it is possible to have an idea of the relative depth of the defects by analyzing the phase contrast profiles. For instance, Fig. 15 presents the phase contrast profiles for the TYPE III defects (excessive adhesive), and Fig. 16 shows the phase contrast profiles for the TYPE IV defects (crushed core). The blind frequency ($f_b \approx 0.2$ Hz) is approximately the same in both cases (as it should since they are located at the same depth). The phase contrast is inverted however for the TYPE III defects (excessive adhesive) given the difference in thermal properties between materials. The adhesive acts like a thermal sink, whilst the air in the TYPE IV defects (crushed core) acts as a thermal resistance. TYPE II defects

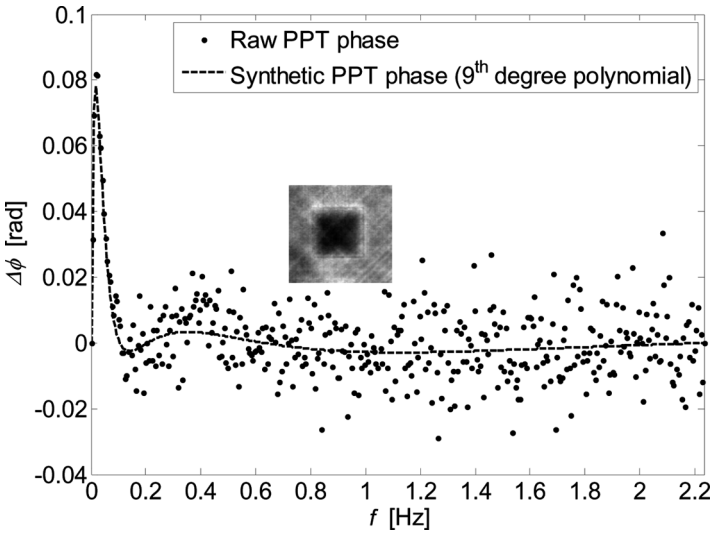

FIGURE 14. Phase contrast profiles for the leftmost TYPE II defect (skin unbonds) in specimen SN043.

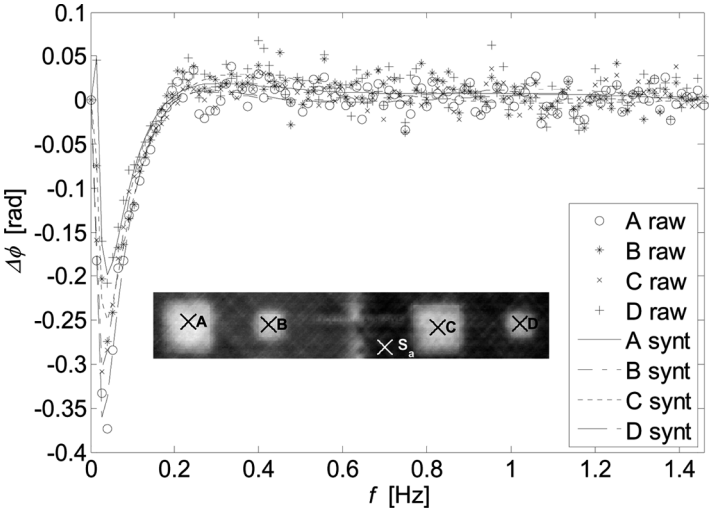

FIGURE 15. Phase contrast profiles for the four TYPE III defect (excessive adhesive) in specimen SN043. Data points correspond to raw data and lines to synthetic data from a 9th degree polynomial.

(core unbonds) should have the same blind frequency and thermal behaviour as the TYPE IV defects. Nevertheless, the estimated blind frequency is in fact half that of the TYPE III and TYPE IV defects. This is possibly due to the high levels of noise (see Fig. 14) that do not allow performing an accurate estimation of the blind frequency.

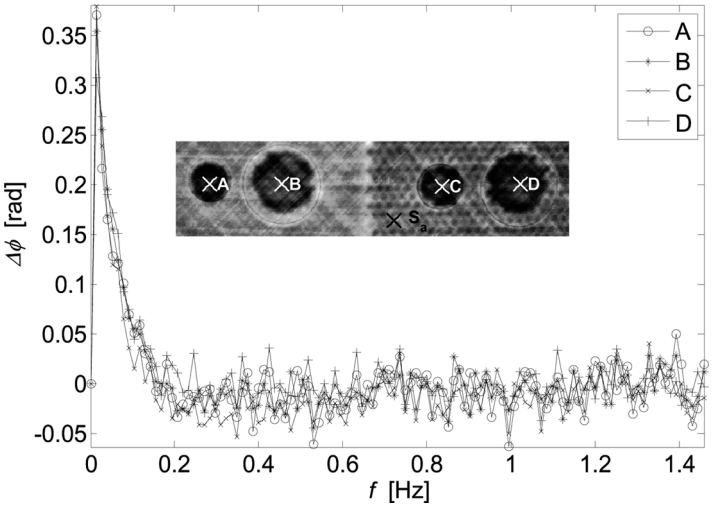

FIGURE 16. Phase contrast profiles for the four TYPE IV defect (crushed core) in specimen SN043.

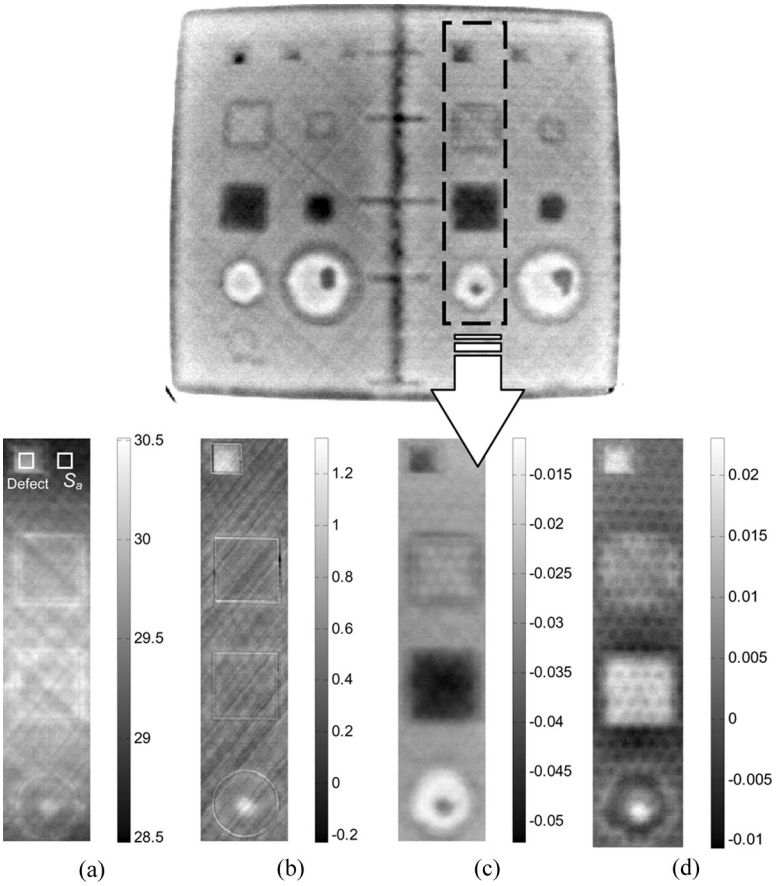

FIGURE 17. Comparative results from PT processing techniques showing maximum SNR for a TYPE I defect (delamination): (a) raw thermogram at $t = 0.7$ s, (b) dac results at $t = 1.0$ s, (c) first time derivative at $t = 2.3$ s, and (d) second time derivative at $t = 3.6$ s.

5.5. SNR Analysis

Figure 17 shows a comparison between raw thermographic data (Fig. 17a) and results from DAC (Fig. 17b) and TSR (Figs. 17c,d) processing. The images were selected for maximum SNR ratio calculated for TYPE I defect (delamination) in the column of defects shown in top of Fig. 17. The SNR was computed as follows:

$$\text{SNR} = \frac{\text{Defect contrast}}{\text{Standard deviation of a reference area}} = \frac{S_{def} - S_{Sa}}{\sigma_{Sa}}, \qquad (19)$$

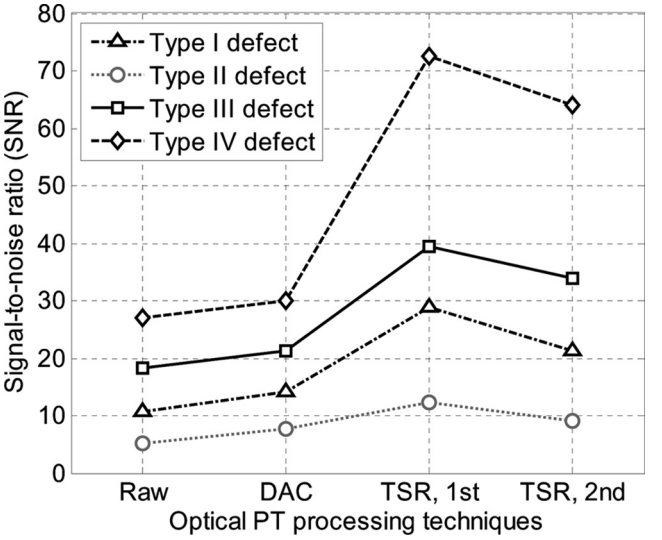

FIGURE 18. Comparison of maximum detectability for all defect types between raw thermographic data and processing results by DAC and TSR.

where S is the signal, either temperature or phase, evaluated in a defective area $_{def}$ or a sound area $_{Sa}$, and σ_{Sa} is the standard deviation in the sound area.

The sound area used for the SNR calculations was calculated as the average value over a 16 pixels x 16 pixels area selected next to the defects. For instance, the defective and sound areas for the TYPE I defect are shown in Fig. 17a. The exact same location was used to estimate the SNR in each processing technique. TYPE I defects are very thin and are located near the surface, they are only visible very early in the sequence. The selection of the time for the ''best'' overall contrast in Fig. 8 was dictated by this particular defect. The other type of defects can be seen at early and later times with varying defect contrast.

Figure 18 shows the SNR for the four defect types in the third column of defects of the SN031 plate (Fig. 17, top) as estimated in the raw thermogram sequence, and in the DAC and TSR (first and second time derivatives) results. As a first observation, SNR is dependent on the defect type: TYPE IV defects (crushed core) have the largest SNR whilst TYPE II defects (skin unbonds) the smallest. And secondly, SNR increases in all cases after processing data by DAC and TSR (especially in first time derivatives), as expected, given that part of the noise is eliminated from the signal.

Figure 19 presents comparative results of the maximum SNR for the three active thermography techniques: VT, LT, and PT. Data in all cases were processed with the DFT. Only one frequency was available in VT

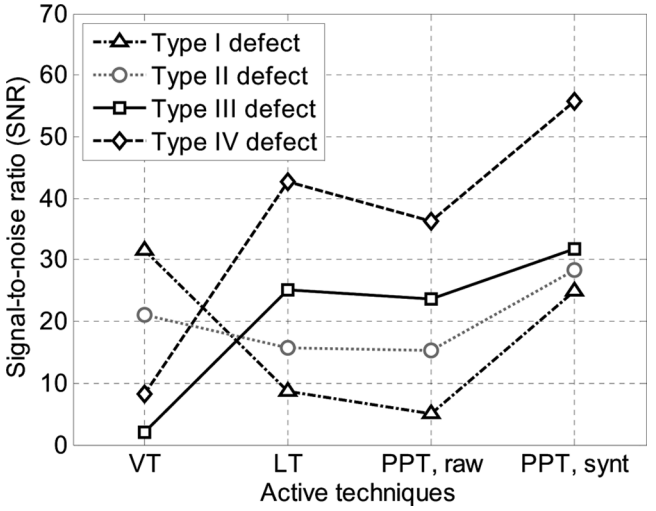

FIGURE 19. Comparative results from all-three active techniques (VT, LT, and PT) showing maximum SNR for the four defect types as indicated.

($f = 2$ Hz) obtained from one experiment, 14 frequencies in LT (from 0.004 to 8 Hz) for the same number of experiments, and 285 frequencies in PT (from 0.0055 to 1.57 Hz) from a single experiment. A general trend is observed when comparing LT and PPT results: LT phasegrams have a slightly better SNR than PPT results obtained from a raw thermogram. However, PPT phasegrams obtained from a synthetic (noiseless) signal reconstructed by TSR, considerably improve their SNR. On the other hand, the SNR of the VT phasegram varies with the defect type; it is higher than any other techniques for the TYPE I and TYPE II defects, but lower for the TYPE III and TYPE IV defects.

The phasegrams at the corresponding frequencies of maximum SNR for the three techniques are shown in Fig. 20. Figure 20a shows the LT phasegram of maximum SNR for the TYPE I defect, Fig. 20b for TYPE II and TYPE III defects and Fig. 20c for TYPE IV defect. The VT phasegram at $f = 2$ Hz (the only frequency tested by VT) is presented in Fig. 20d. PPT phasegrams obtained by TSR (7th degree polynomial fitting) are shown in Figs. 20e–h, and correspond to the maximum SNR for TYPE I to TYPE IV defects, respectively. PPT phasegrams obtained from raw thermograms (not shown) are very similar to the synthetic but they are contaminated by noise. The maximum SNR for the TYPE I defects (delaminations) is obtained at a much higher frequency (Fig. 20e) than the other three types of defects (Fig. 20f–h). Although defects TYPE II to IV are all at the same depth, the frequency of maximum SNR is different from the others, confirming that defect visibility depends on the defect type.

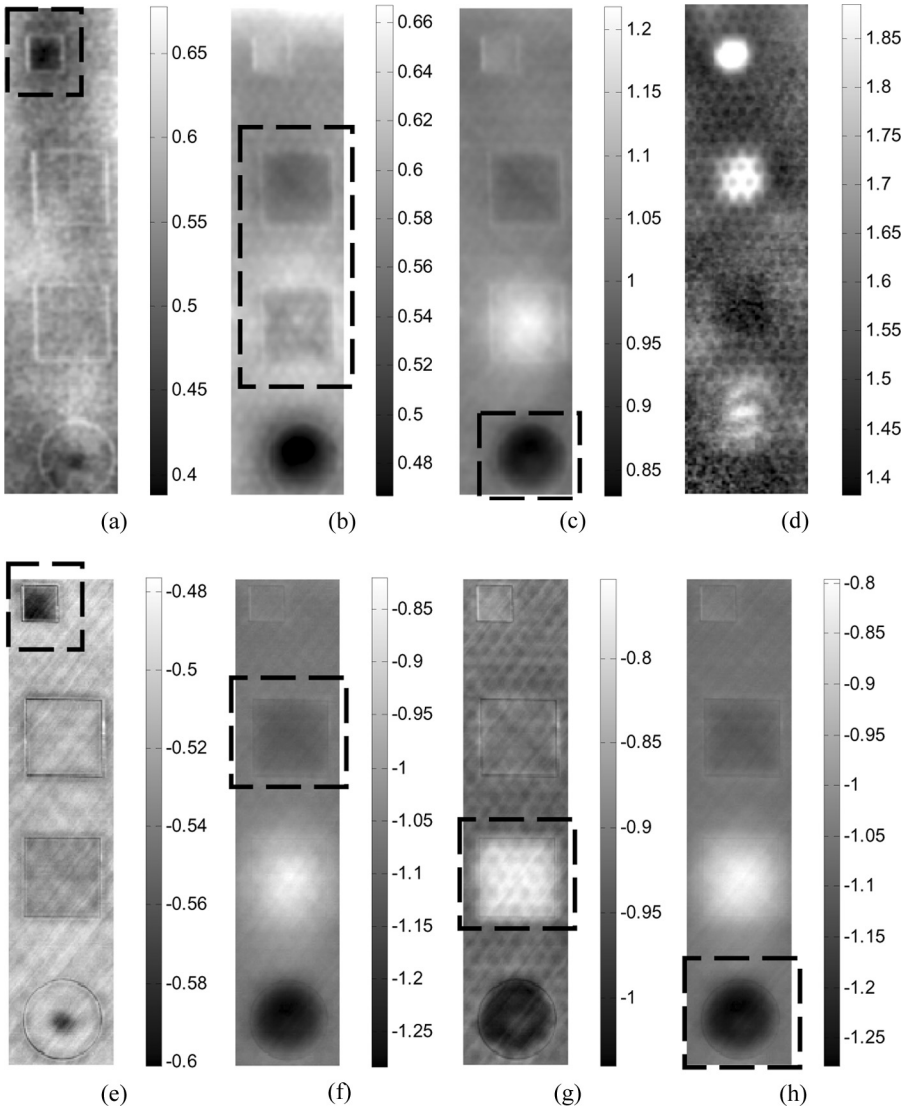

FIGURE 20. Top: maximum SNR for (a) TYPE I defect by lt at $f = 2$ Hz, (b) TYPE II and II defects by LT at $f = 0.01$ Hz, (c) TYPE IV defect by LT at $f = 0.02$ Hz, and all defect types by VT at $f = 2$ Hz. Bottom: PPT synthetic phasegrams (calculated from a 7th degree polynomial by TSR) of maximum detectability for (e) TYPE I defect (delamination) at $f = 0.36$ Hz, (f) TYPE II defect (skin unbonds) at $f = 0.011$ Hz, (g) TYPE III defect (excessive adhesive) at $f = 0.006$ Hz, and (h) TYPE IV defect (crushed core) at $f = 0.028$ Hz.

6. CONCLUSIONS

In this study, two honeycomb core calibration specimens used as standards in the NDE of aerospace parts were inspected by PT, LT, and VT under laboratory conditions. From this investigation it can be concluded that these three active thermography techniques can be used for the NDE assessment of honeycomb sandwich structures.

PT is fast and easy to deploy [52,53]. Although data is affected by different problems (nonuniform heating, emissivity variations, environmental reflections, and surface geometry), there are numerous processing techniques available to counter these and therefore obtain prompt results of reliable quality, as well as quantitative information (in some instances).

LT allows a better control of the energy deposited on a surface. LT requires a separate experiment for each and every inspected depth, and there is a stabilization time before reaching a steady-state regime. Hence, inspection by LT is in general slower than other approaches such as PT. A complete LT experiment is carried out by inspecting the specimen at several frequencies, covering a wide range from low to high frequencies, and then a fitting function can be used to complete the amplitude or phase profiles for each point (or pixel). Nevertheless, there exists a direct relationship between the depth and the inspection frequency that allows defect characterization to be performed from the amplitude or phase data without further processing. Furthermore, the energy required to perform an LT experiment is generally less than in other active techniques, which might be interesting if a low power source is to be used or if special care has to be given to the inspected part.

VT is still lacking of quantitative studies, and very often optimal inspection parameters must be found experimentally. In either lock-in or burst configuration, VT is extremely fast, although it is necessary to relocate the transducer (and to immobilize the specimen again) to cover a large area for inspection. Hence, VT is more suitable for relatively small objects. But probably the most inconvenient aspect of VT is the need for a coupling media between the sample and the transducer, and the need for holding the specimen. On the other hand, there is only minimal heating of the inspected specimen since the energy is usually dissipated mostly at the defective areas, although there is some localized heating at the coupling and clamping points.

An SNR analysis allows comparing the quality of processing of the different PT techniques and between active approaches (PT, LT, and LT). For instance, processing pulsed data by TSR considerably reduces noise, increasing SNR and defect visibility. The maximum SNR for a particular defect was observed in the first time derivative images. An increase in SNR was also observed when using the DAC technique, although the increase was less pronounced. It should be pointed out however that the nonuniformity of the background plays an important role that is not taken into consideration in the estimation of SNR in Eq. (18). A highly nonuniformly heated specimen could produce a high SNR simply because a high temperature difference

exists between two regions. The DAC technique reduces the nonuniformities of heating on the surface, resulting in a decrease in contrast in some regions, which means that the increase in SNR with respect to raw data is due to an improvement in signal variability (standard deviation).

The difference in SNR between active techniques depends on the type of defect. In general, LT phasegrams produce higher SNR than PPT, although PPT results are considerably improved when working with synthetic data (from a TSR experiment). On the other hand, VT produced high SNR for two defect types (delaminations and skin unbonds) and low SNR for the other two (excessive adhesive and crushed core).

Finally, depth retrieval is possible using phase data obtained by PPT. However, accurate estimations are only possible for single layer materials. Steps are undertaken to extend the PPT quantitative approach for a multilayer structures by combining the PPT algorithm with the thermal quadrupoles theory.

ACKNOWLEDGMENTS

This work has been supported by the grant from the Canada Research Program (CRC): Multipolar Infrared Vision Canada Research Chair (MiViM). Acknowledgments are attributed to TWI's Technology Centre in South Wales, UK as part of this research study was completed in the NDT Centre; to Harold Hebert who kindly agree to perform the c-scan tests over one of the samples at the Industrial Materials Institute in Boucherville, Quebec; and to the National Research Council of Canada for its financial support.

REFERENCES

1. H. S. Carslaw and J. C. Jaeger. *Conduction of Heat in Solids*, 2nd edition. Clarendon Press, Oxford (1986).
2. R. Bracewell. *The Fourier Transform and its Applications*. McGraw-Hill, Toronto (1965).
3. X. Maldague, A. Ziadi, and M. Klein. *NDT and E Int.* **37(7)**:559–564 (2004).
4. X. P. V. Maldague. *Theory and Practice of Infrared Technology for Nondestructive Testing*. John Wiley-Interscience, New York (2001).
5. C. Ibarra-Castanedo, A. Bendada, and X. Maldague. *GESTS Int'l Trans. Computer Science and Engr.* **22(1)**:89–100 (2005).
6. C. Ibarra-Castanedo, D. González, M. Klein, M. Pilla, S. Vallerand, and X. Maldague. *Infrared Phys. Technol.* **46(1–2)**:75–83 (2004).
7. C. Ibarra-Castanedo, M. Genest, P. Servais, X. Maldague, and A. Bendada. *NDT & E* **22(2–3)**:199–215 (2007).
8. R. E. Marti, A. L. Gyekenyesi, and S. M. Shepard. *Mater. Eval.* **61(5)**:611–616 (2003).
9. M. Pilla, M. Klein, X. Maldague, and A. Salerno. *Proc. QIRT* **6**:53–58 (2002).
10. M. Pilla, *Ph.D. Thesis*. Politecnico di Milano. Milan, Italy (2002).
11. M. Klein, M. Pilla, and X. Maldague. MATLAB script for advance processing of pulsed infrared data. Laval University, Quebec City, Canada. Available online at http://vision.gel.ulaval.ca/~klein/ir_view/ir_view_doc.htm [Accessed December 29, 2008].
12. D. A. González, C. Ibarra-Castanedo, M. Pilla, M. Klein, J. M. López-Higuera, and X. Maldague. *Proc. QIRT* **7**:H.16.1–H.16.6 (2004).

13. H. D. Benítez, C. Ibarra-Castanedo, A. Bendada, X. P. Maldague, H. Loaiza, and E. Caicedo. *Infrared Phys. Technol.* (accepted for publication).
14. S. M. Shepard. *Proc. SPIE: Thermosense XXVIII* **4360**:511–515 (2001).
15. S. M. Shepard. *Insight* **43(9)**:587–589 (2001).
16. S. M. Shepard, J. R. Lhota, B. A. Rubadeux, T. Ahmed, and D. Wang. *SPIE: Thermosense XXVII* **4710**:531–535 (2002).
17. X. P. Maldague and S. Marinetti. *J. Appl. Phys.* **79(5)**:2694–2698 (1996).
18. X. Maldague and J.-P. Couturier. *Proc. AITA* **53(1)**:271–286 (1997).
19. C. Ibarra-Castanedo and X. Maldague. *QIRT J.* **1(1)**:47–70 (2004).
20. J. W. Cooley and J. W. Tukey. *Mathematics of Computation* **19(90)**:297–301 (1965).
21. A. Dillenz, T. Zweschper, and G. Busse. *SPIE: Thermosense XXVIII* **4360**:574–579 (2001).
22. C. Ibarra-Castanedo, Ph.D. thesis, Laval University, Quebec City, QC, Canada (2005). Available at http://www.theses.ulaval.ca/cocoon/meta/2005/23016.xml [Accessed December 29, 2008].
23. C. Ibarra-Castanedo, D. González, and X. Maldague. *Proc. 16th WCNDT [CD]. CINDE-ICNDT* (2004).
24. C. Ibarra-Castanedo, N. P. Avdelidis, and X. Maldague. *Mater. Eval.* **63(11)**:1128–1133 (2005).
25. C. Ibarra-Castanedo and X. Maldague. *Res. Nondestr. Eval.* **16(4)**:1–19 (2005).
26. F. Galmiche, S. Vallerand, and X. Maldague. In *Review of Progress in Quantitative NDE*, D. O. Thompson and D. E. Chimenti (eds.), vol. 19A, pp. 609–615 (2000). American Institute of Physics.
27. G. Zauner, G. Mayr, and G. Hendorfer. *SPIE:Wavelet Applications in Industrial Processing IV* **6383**:0E (2006).
28. C. Ibarra-Castanedo, D. A. González, F. Galmiche, A. Bendada, and X. Maldague. *Recent Res. Devel. Applied Phys.* **9**:101–127 (2006).
29. N. Rajic. *Compos. Struct.* **58**:521–528 (2002).
30. S. Marinetti, E. Grinzato, P. G. Bison, E. Bozzi, M. Chimenti, G. Pieri, and O. Salvetti. *Infrared Phys. and Technol.* **46**:85–91 (2004).
31. C. Ibarra-Castanedo, D. González, F. Galmiche, X. P. Maldague, and A. Bendada. *SPIE: Thermosense XXVIII* **6205**:14 (2006).
32. G. Giorleo and C. Meola. *NDT and E. Int.* **35**:287–292 (2002).
33. P. E. Nordal and S. O. Kanstand. *Physica Scripta* **20**:659–662 (1979).
34. G. Busse. In *Nondestructive Handbook, Infrared and Thermal Testing*, X. Maldague Technical ed., P. O. Moore ed., 3rd ed. **3** (2001).
35. D. Wu and G. Busse. *Rev. Gén. Therm.* **37**:693–703 (1998).
36. L. D. Favro and X. Han. In *Sensing for Materials Characterization, Processing and Manufacuring*, G. Birnbaum and B. A. Auld (eds.), Vol. 1, pp. 399–415 (1998). ASNT TONES.
37. G. Busse, D. Wu, and W. Karpen. *J. Appl. Phys.* **71(8)**:3962–3965 (1992).
38. J. C. Krapez. *Proc. QIRT* **4**:148–153 (1998).
39. W. Bai and B. S. Wong. *Meas. Sci. Technol.* **12**:142–150 (2001).
40. G. Busse. *Appl. Phys. Lett.* **35**:759 (1979).
41. G. Busse. *NDT&E Int.* **27(5)**:253–262 (1994).
42. G. Busse and A. Rosencwaig. *Appl. Phys. Lett.* **36(10)**:815–816 (1980).
43. C. Meola and G. M. Carlomagno. *Meas. Sci. Technol.* **15**:27–58 (2004).
44. C. Meola, G. M. Carlomagno, and G. Giorleo. *J. Mater. Process. Technol.* **155–156**:1132–1137 (2004).
45. R. L. Thomas, J. J. Pouch, Y. H. Wong, L. D. Favro, and P. K. Kuo. *J. Appl. Phys.* **51(2)**:1152–1156 (1980).
46. L. D. Favro, X. Han, Z. Ouyang, G. Sun, H. Suiand, and R. L. Thomas. *Rev. Sci. Instr.* **71(6)**:2418–2421 (2000).
47. G. Busse. *Applied Optics* **21(1)**:107–110 (1982).
48. R. L. Thomas. In *Review of Quantitative Nondestructive Evaluation*, D. O. Thompson and D. E. Chimenti (eds.), **21**:3–13 (2002).
49. S. K. Sinha, S. R. Iyer, and M. C. Bhardwaj. *Proceedings of IEEE Sensors* **2(1)**:493–498 (2003).
50. T. Zweschper, G. Riegert, A. Dillenz, and G. Busse. *SPIE: Thermosense XXV* **5073**:386–391 (2003).
51. S. M. Shepard, T. Ahmed, and J. R. Lhota. *SPIE: Thermosense XXVI* **5405**:332–335 (2004).
52. N. P. Avdelidis, D. P. Almond, A. Dobbinson, B. C. Hawtin, C. I. barra-Castanedo, and X. Maldague. *Progress in Aerospace Sciences* **40(3)**:143–162 (2004).
53. N. P. Avdelidis, B. C. Hawtin, and D. P. Almond. *NDT and E. Int.* **36(6)**:433–439 (2003).